SEDIMENTOLOGY the journal of the International Association of Sedimentologists

*Sedimentology* (2022) **69**, 282–300 doi: 10.1111/sed.12927

# Shallow-marine carbonate cementation in Holocene segments of the calcifying green alga *Halimeda*

THOMAS MANN*,†,[1], ANDRÉ WIZEMANN*,‡,[1], MARLEEN STUHR*,§,¶, YANNIS KAPPELMANN*,**, ALEXANDER JANßEN*,**, JAMALUDDIN JOMPA†† and HILDEGARD WESTPHAL*,**

**Leibniz Centre for Tropical Marine Research (ZMT), Fahrenheitstraße 6, Bremen, Germany (E-mail: thomas.mann@bgr.de)*

*†Bundesanstalt für Geowissenschaften und Rohstoffe (BGR), Stilleweg 2, Hannover, Germany*

*‡Bioplan GmbH, Strandstraße 32a,Ostseebad, Nienhagen, 18211, Germany*

*§Interuniversity Institute for Marine Sciences (IUI), Eilat, Israel*

*¶Bar-Ilan University (BIU), Ramat Gan, Israel*

***University of Bremen, Bibliothekstraße 1, Bremen, Germany*

*††Hasanuddin University, Jl. Perintis Kemerdekaan KM.10, Makassar, Indonesia*

Associate Editor – Guillem Mateu-Vicens

## ABSTRACT

Early-diagenetic cementation of tropical carbonates results from the combination of numerous physico-chemical and biological processes. In the marine phreatic environment it represents an essential mechanism for the development and stabilization of carbonate platforms. However, diagenetic cements that developed early in the marine phreatic environment are likely to become obliterated during later stages of meteoric or burial diagenesis. When lithified sediment samples are studied, this complicates the recognition of processes involved in early cementation, and their geological implications. In this contribution, a petrographic microfacies analysis of Holocene *Halimeda* segments collected on a coral island in the Spermonde Archipelago, Indonesia, is presented. Through electron microscopical analyses of polished samples, this study shows that segments are characterized by intragranular cementation of fibrous aragonite, equant High-Mg calcite (3.9 to 7.2 Mol% Mg), bladed Low-Mg calcite (0.4 to 1.0 Mol% Mg) and mini-micritic Low-Mg calcite (3.2 to 3.3 Mol% Mg). The co-existence and consecutive development of fibrous aragonite and equant High-Mg calcite results initially from the flow of oversaturated seawater along the aragonite template of the *Halimeda* skeleton, followed by an adjustment of cement mineralogy towards High-Mg calcite as a result of reduced permeability and fluid flow rates in the pores. Growth of bladed Low-Mg calcite cements on top of etched substrates of equant High-Mg calcite is explained by shifts in pore water pH and alkalinity through microbial sulphate reduction. Microbial activity appears to be the main trigger for the precipitation of mini-micritic Low-Mg calcite as well, based on the presumable detection of an extracellular polymeric matrix during an early stage of mini-micrite Low-Mg calcite cement precipitation. Radiocarbon analyses of five *Halimeda* segments furthermore indicate that virtually complete intragranular cementation in the marine phreatic environment with thermodynamically/kinetically controlled aragonite and High-Mg calcite takes place in about 100 years. Collectively,

[1]These authors contributed equally to this work.

this study shows that early-diagenetic cements are highly diverse and provides new quantitative constraints on the rate of diagenetic cementation in tropical carbonate factories.

**Keywords** Cementation rate, low-Mg calcite cementation, marine diagenesis, microbial sulphate reduction, permeability, porosity, tropical carbonates.

## INTRODUCTION

During Earth history, alternating major framework builders and carbonate sediment producers have created the most diverse ecosystems in the oceans, however many internal processes and controls of carbonate platform development remain enigmatic (Pomar, 2001; Melim *et al.*, 2002; Pomar & Hallock, 2008; Pomar & Kendall, 2008; Pomar *et al.*, 2012a). To better understand the evolution of carbonate platforms through time, it is important to also recognize rather cryptic and small-scale processes, because these are essential for the functioning of carbonate ecosystems in the larger context (Pomar *et al.*, 2004; Pomar *et al.*, 2012b; Pomar & Haq, 2016; Pomar *et al.*, 2017). One example for such a process addressed here is the early-diagenetic cementation of shallow-marine carbonate detritus in tropical reef environments.

Early-diagenetic carbonate cementation in tropical reef environments is controlled by a combination of abiotic and biotic factors (Bathurst, 1971; Tucker & Bathurst, 1990; Burton, 1993; Flügel, 2004). Abiotic factors include seawater and pore-water carbonate chemistry, primary porosity, fluid flow rates, and the mineralogy of the substrate (Shinn, 1969; Folk, 1974; Longman, 1980; Given & Wilkinson, 1985; Henrich & Wefer, 1986; Morse *et al.*, 2007). Biotic factors comprise influences such as microorganismal colonization, micro-bioerosion and microbial activity (Bathurst, 1966; Kendall & Skipwith, 1969; Reid & Macintyre, 2000; Summons *et al.*, 2013; Wizemann *et al.*, 2018). The interplay of these controls on early-diagenetic carbonate cementation triggers the occurrence of multiple generations of cements in conjunction with variable crystal shapes and mineralogy.

Prominent constituents in modern detrital carbonate sediments are the segments of the benthic calcareous green macro-alga genus *Halimeda* (Hillis-Colinvaux, 1980; Johns & Moore, 1988; Multer, 1988; Rees *et al.*, 2007). Most detrital *Halimeda* segments accumulating in shallow-water settings such as sand shoals and beaches belong to lithophytic species like *Halimeda opuntia* that produce well-calcified segments and grow preferentially in fore-reef and reef-crest environments, or on patch reefs on reef flats (Wizemann *et al.*, 2015).

*Halimeda* segments exhibit a complex and porous microstructure (Fig. 1). In the pristine state during lifetime and immediately after disaggregation from the living alga, segments of *Halimeda* consist of a mesh of fibrous aragonite crystals surrounding spherical to elliptical pores referred to as utricles. The algal cells during lifetime reside in those utricles that stabilize the segment through calcification (Wizemann *et al.*, 2014). During this process, the space between the utricles becomes successively filled with fibrous aragonite, specifically with: (i) primary needles at utricle walls; (ii) secondary needles in interutricular spaces; and (iii) micro-anhedral carbonate (i.e. primary aragonite cements) along utricle rims (see Wizemann *et al.*, 2014, for more details). The resulting microstructure of a *H. opuntia* segment displays a densely calcified primary interutricular space along the outer rim, and a less strongly calcified secondary interutricular space towards the segment centre.

For reconstructing the diagenetic processes it is relevant to note that the pristine skeleton of a *Halimeda* segment is composed of the carbonate polymorph aragonite only, and that the utricles and the interutricular space represent two largely separated microenvironments in detrital *Halimeda* segments with the utricles representing open pore space. These utricles are then accessible to circumfluent seawater, whereas the interutricular space is usually more isolated from the surrounding environment with only minor exchange and circulation between seawater and pore-water (Wizemann *et al.*, 2014).

Diagenetic aragonite precipitated as cement in utricles is a common feature in detrital segments and is usually interpreted as abiotic growth of fibrous aragonite crystals on the utricle walls (Reid & Macintyre, 1998; Hover *et al.*, 2001). In

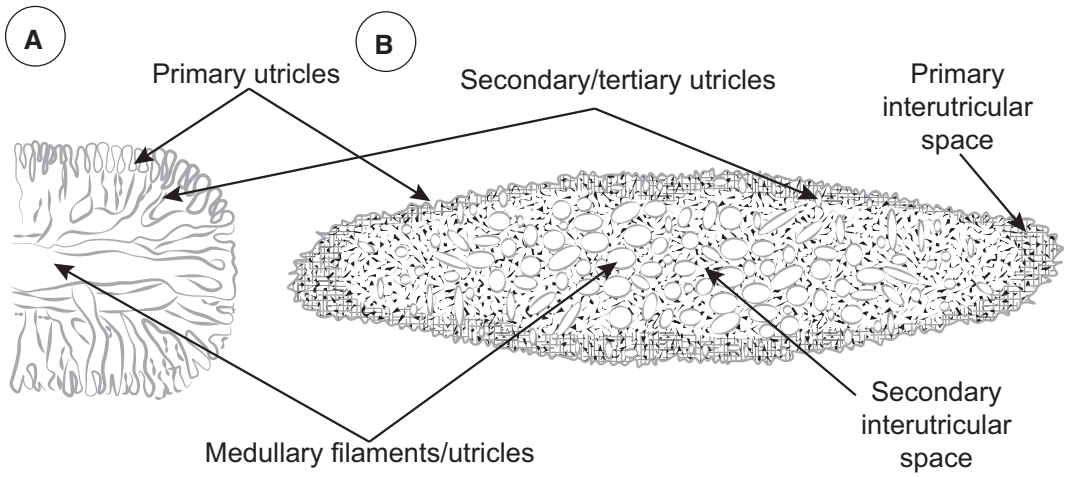


**Fig. 1.** Conceptual illustrations showing the complex internal microstructure of a pristine segment of the species *Halimeda opuntia*: (A) Longitudinal section; and (B) cross-section through an apical segment (adapted from Hillis-Colinvaux, 1980; Wizemann *et al.*, 2014).

pre-Holocene segments, cementation of utricles with blocky calcite cements is also commonly observed, often in conjunction with dissolution of the original aragonite skeleton (Scholle & Ulmer-Scholle, 2003; Flügel, 2004). Such neomorphoses, replacing the original aragonite, form under the influence of meteoric waters or during shallow-marine burial diagenesis (Melim *et al.*, 2004).

While intragranular calcite cementation is well-known for late-diagenetically altered *Halimeda* segments because of their primary aragonite skeleton mineralogy, only few studies have documented the onset of such diagenetic patterns in close-to-pristine segments from modern marine depositional environments. For example, published reports on High-Mg calcite cementation in *Halimeda* segments are limited to descriptions from the Brazilian shelf (Alexandersson & Milliman, 1981), reef sediments of Belize (Reid & Macintyre, 1998) and *Halimeda* bioherms from the Java Sea (Roberts *et al.*, 1988). In these studies, High-Mg calcite cementation is interpreted to reflect physico-chemical changes in seawater parameters through time. Reports on intragranular Low-Mg calcite cementation within modern *Halimeda* segments are, to our knowledge, lacking.

The present study describes the occurrence of: (i) fibrous; (ii) equant; (iii) bladed; and (iv) minimicritic Holocene carbonate cements in shallow-marine, detrital *Halimeda* segments collected from a reef island in the Spermonde Archipelago, Indonesia. The aim of this study is to decipher the processes related to early-diagenetic aragonite and calcite cementation, and their temporal implications.

## STUDY SITE

The Spermonde Archipelago is a rimmed carbonate shelf attached to the West coast of Sulawesi with numerous islands sprinkled on the platform (Fig. 2; Umbgrove, 1928; Renema & Troelstra, 2001; Kench & Mann, 2017). In the mid-Holocene (*ca* 3–6 ka BP) the carbonate platform experienced a relative sea-level highstand likely not exceeding *ca* 0.5 m above present sea-level (Mann *et al.*, 2016; Mann *et al.*, 2019; Bender *et al.*, 2020). The island studied here, Pulau Panambungan, is a vegetated sand cay of some 170 m in diameter, almost circular in shape and fringed by a concentric reef flat. Some huts and remnants of houses indicate the occasional presence of daily tourists; however, besides that the island is uninhabited and appears abandoned. Morphological characteristics comprise a beach berm that is more pronounced on the western, windward side of the island, and a central depression (Fig. 3). These characteristics are similar to other coral reef islands in the Indo-Pacific region (Woodroffe *et al.*, 1999; Kench *et al.*, 2005; Kench *et al.*, 2014). Pulau Panambungan is composed of sand-sized and gravel-sized sediments with only minor finer-grained

fractions, and is dominated by reworked fragments of crustose coralline algae and corals (Janßen *et al.*, 2017).

## MATERIAL AND METHODS

### Sampling and sample processing

Forty bulk surface sediment samples from the upper *ca* 5 cm of the nearshore reef flat and the island have been collected along four transects across Pulau Panambungan (Fig. 2). Additionally, 42 subsurface sediment samples from excavations down to *ca* 1.25 m were taken in the central and marginal island sections (Janßen *et al.*, 2017). Samples collected from the island margins (Profiles 1–3 in Figs 2C and 3) were taken from elevations between low and high tide levels (Fig. 3). Samples from the central profile were taken from above the freshwater table and thus belong to the meteoric vadose diagenetic environment. All sediment samples collected were unlithified.

The sediment samples, each weighing *ca* 200 g, were cleaned in the laboratory with deionized water and then oven-dried at 40°C for 48 h. Subsequently, samples were sieved according to the grain-size classes of Wentworth (1922), and each fraction was analyzed with respect to compositional characteristics (see Janßen *et al.*, 2017, for more details on the facies reconstruction).

For the present study, the calcirudite fraction (>1 mm) of the 82 sediment samples was screened for *Halimeda* segments in a picking tray under a binocular microscope. In 27 samples (*ca* 33%), *Halimeda* segments were identified (three surface and 24 subsurface samples, see Figs 2 and 3).

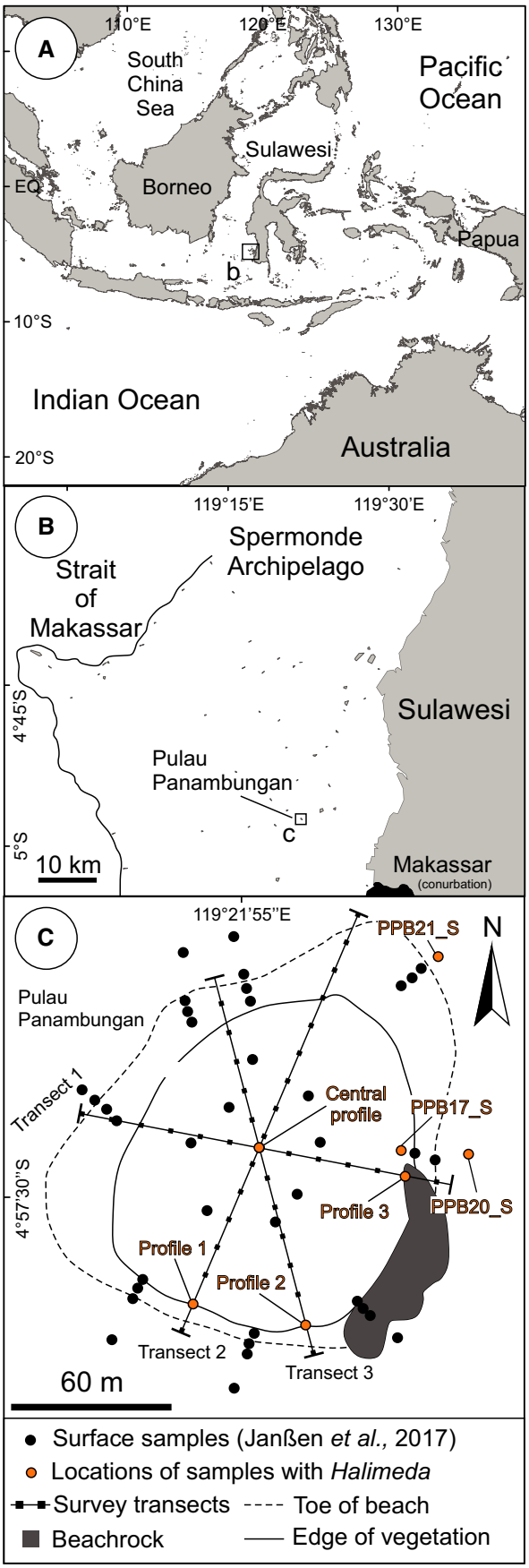


**Fig. 2.** Location of the study site in Indonesia. (A) Overview map indicating the geographic position of the Spermonde Archipelago at the west coast of south-west Sulawesi. (B) Map of the Spermonde Archipelago showing the location of the study island Pulau Panambungan on the carbonate shelf. Black line indicates position of the discontinuous barrier reef. (C) Detailed map of the study island in plan view, based on a shoreline survey in October 2012, indicating the exact positions of surface sediment samples, profiles and survey transects.

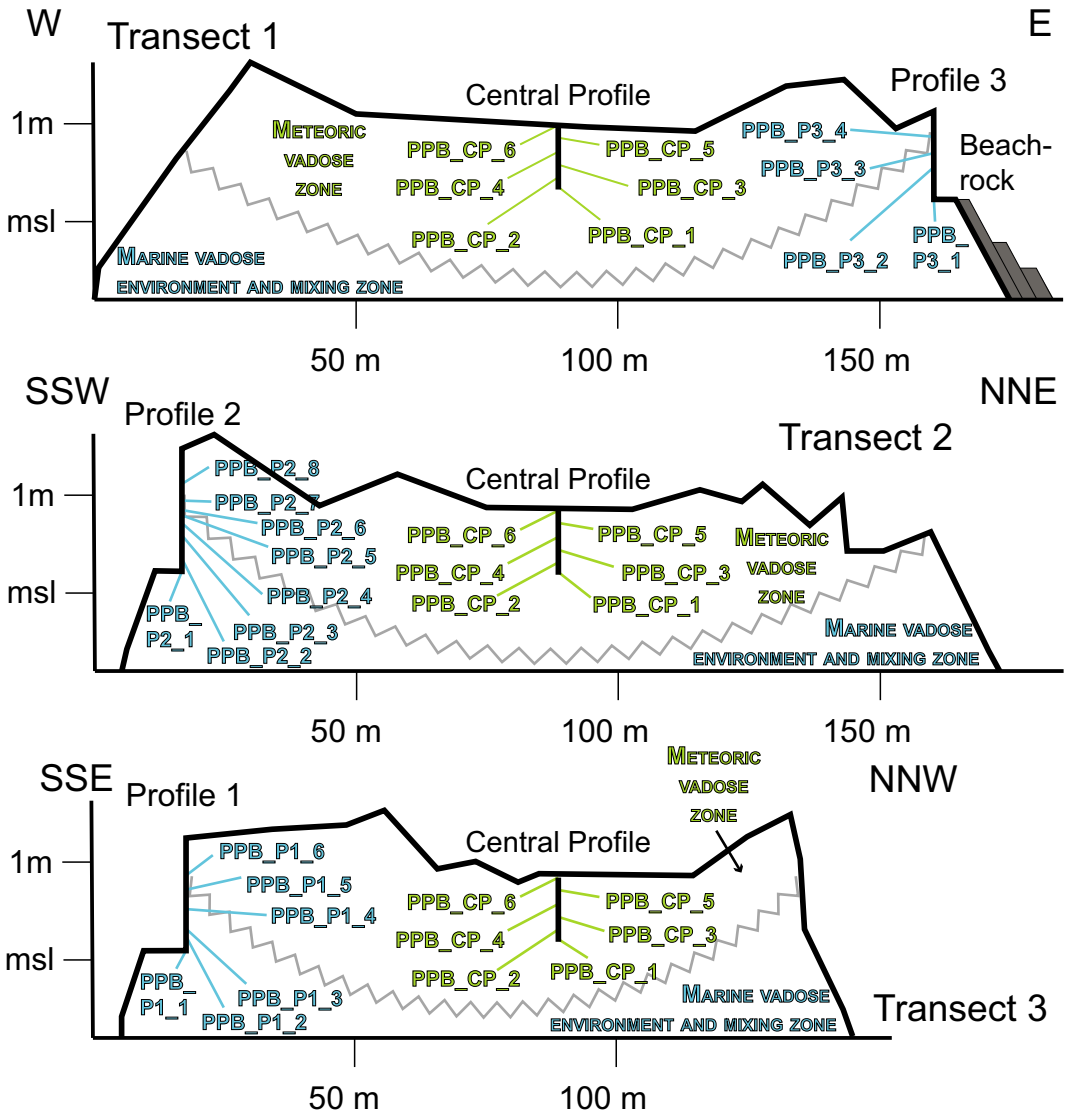


**Fig. 3.** Topographic transects across Pulau Panambungan indicating the slightly higher elevation of western island margins, the central morphological depression and the positions of subsurface sediment samples examined in this study. Note that the positions of subsurface sediment samples are not exactly to scale to allow for better readability. Detailed information on sample depths can be found in Janßen *et al.* (2017). Island elevation has been surveyed with an optical level and reduced to mean sea level derived from measurements of water level loggers (Mann *et al.*, 2016). The boundary between the diagenetic zones has been estimated from the maximum tidal range of *ca* 1.5 m in that area.

## Scanning electron microscope analyses

For investigating the diagenesis within segments of *Halimeda*, they were cut to polished sections. The polished surfaces were gold-sputtered and subsequently analyzed with a scanning electron microscope (SEM; TESCAN Vega3-XMU; TESCAN, Orsay, Czech Republic) at 10 keV in the backscattered electron mode to determine the mineralogy of the carbonate cements.

Crystal shapes of carbonate cements in the utricles were classified according to the Folk (1965) terminology, comprising: (i) fibrous crystals with length to width ratios >6 : 1; (ii) equant crystals with length to width ratios <1.5 : 1; and (iii) bladed crystals with intermediate length to width ratios. Additionally, the shape of crystal terminations, crystal appearance and the growth relation of crystals and substrate are described (Flügel, 2004).

In order to obtain the information on the cement mineralogy necessary for reconstructing the interplay of processes affecting carbonate diagenesis, this study applied a three-step approach. First, the brightness of cements was compared visually to the appearance of the original aragonite skeleton in backscattered SEM images in order to identify differences in mineralogy (Reid & Macintyre, 1998; Reid & Macintyre, 2000; Wizemann *et al.*, 2015; Gacutan *et al.*, 2017).

Where grey-scales differed between cements and the original aragonite skeleton, the concentration of Mg in the specific areas was determined by energy dispersive X-ray (EDX), assuming that the Mg content of carbonates is a good indicator for the differentiation between common carbonate polymorphs, as Mg replaces Ca mostly in the calcite crystal lattice. EDX element maps were obtained at 10 keV with an Oxford 50 $mm^2$ X-ray element detector (Oxford Instruments, Abingdon, UK). For each element distribution map, the samples were scanned continuously at 50 μs $pixel^{-1}$ for *ca* 20 min. The resulting maps were subsequently interpolated by 3 × 3 pixels with the EDX software Aztec (Oxford Instruments) to enhance the resulting image.

Where element distribution maps indicated a higher concentration of Mg in cements, point EDX measurements were used to determine the Mg content. Element spectra were obtained at *ca* 100 k counts per point measurement at 10 keV, while beam intensity (i.e. excitation energy) was kept low for restricting the area measured to <10 $\mu m^2$, thus avoiding overlaps to other materials. The resulting element graphs were normalized, gold detected from gold sputtering (at *ca* 2.2 keV) was excluded by auto ID and the noise peak was removed. The spectra were quantified using the Aztec Software to determine the concentration of Mg that was then converted to Mol% in the calcium carbonate.

### Radiocarbon dating

For age control, the bisected halves of five analyzed segments were radiocarbon-dated. The $^{14}C$ ages were calibrated to calendar years before present (cal yr BP) using the Marine20 radiocarbon age calibration curve with a ΔR of −64 ± 70 $^{14}C$ years as closest estimate for the Southern Makassar Strait (Southon *et al.*, 2002).

## RESULTS

### Fibrous cements

Fibrous crystals partly or completely infilling the utricles were observed in seven specimens (PPB_CP3, PPB_CP4, PPB_P2_1, PPB_P2_3, PPB_P2_4, PPB_P2_6 and PPB_P1_4; see Fig. 4). These fibrous crystals are characterized by a prismatic shape with a length up to *ca* 20 μm and a width between 0.5 μm and 2.0 μm. Crystals appear clear without notable inclusions and are characterized by rather blunt terminations. There is no distinct boundary between the fibrous cements in the utricles and the primary needles that develop during the lifetime of the segment along the utricle walls.

Fibrous carbonate cements with a prismatic crystal habit exhibit a similar brightness of grey-scales in backscattered SEM images as the original aragonitic skeleton of the segments (Fig. 4B). An EDX point measurement in the centre of a fibrous cement-filled utricle of specimen PPB_P2_6 shows no indication of Mg, pointing to an aragonitic mineralogy.

### Equant cements

Equant carbonate crystals within utricles have been detected in 14 specimens (PPB_17S, PPB_CP_3, PPB_CP_4, PPB_CP_5, PPB_P3_1, PPB_P3_2, PPB_P2_1, PPB_P2_3, PPB_P2_4, PPB_P2_6, PPB_P2_7, PPB_P2_8, PPB_P1_3 and PPB_P1_4; see Fig. 5). These rhombohedral cements show nearly equidimensional crystal edges of 1 to 5 μm in length. Terminations of the crystals are sharply pointed, and surfaces appear either clear or, to a variable degree, corroded. They grow on top of crystals of the utricle walls and embed primary needles and fibrous aragonite cements (Fig. 5H).

Equant carbonate cements exhibit distinctly darker grey-scales in backscattered SEM images than the surrounding aragonitic interutricular space (Fig. 5), pointing to a different carbonate polymorph than aragonite. EDX element maps indicate higher concentrations of Mg than for the surrounding aragonite as confirmed by EDX point measurements that show 3.9 to 7.2 Mol% Mg ($n$ = 10; Table 1). Therefore, the equant cements are thought to consist predominantly of High-Mg calcite, close to the boundary between High-Mg and Low-Mg calcite (Burton, 1993; Flügel, 2004).

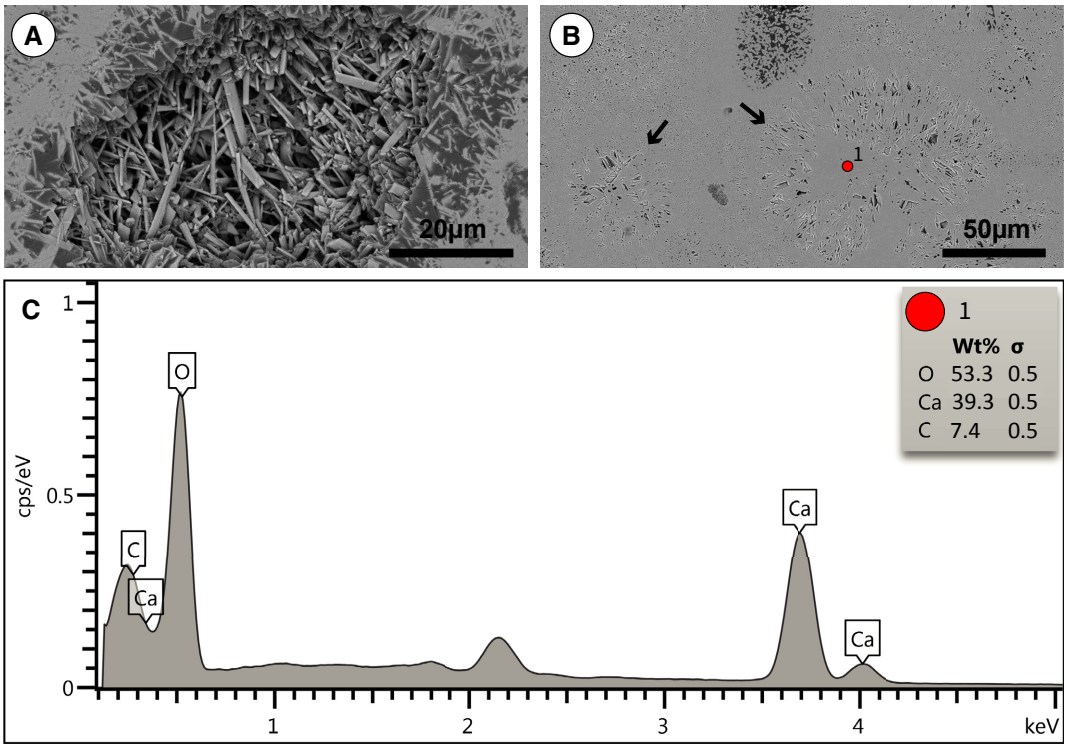


**Fig. 4.** Examples for aragonite cementation in utricles of *Halimeda*. (A) Backscattered electron image of a utricle of specimen PPB_P2_3 showing complete cementation with fibrous aragonite cements. (B) Backscattered electron image of a utricle of specimen PPB_P2_6 showing that fibrous aragonite-cemented utricles exhibit the same grey-scales as the surrounding original microstructure. Red point indicates measurement spot of EDX spectrum shown in (C). Black arrows indicate utricle rims. (C) EDX spectrum from a measurement of fibrous aragonite cements – red point in (B) – indicate that the fibrous cements do not contain Mg (see also Table 1).

## Bladed cement

Bladed cements within utricles have been detected merely in specimen PPB_CP_3 (Fig. 6). These scalenohedral cements show lengths between 25 µm and 45 µm and widths between 10 µm and 30 µm. Terminations are pointed and crystal surfaces appear clear. The bladed cements grow on top of equant High-Mg calcite cements with a distinctly corroded boundary in between (Fig. 6C and D). Backscattered SEM images show strong differences of grey-scales between: (i) the bladed cements; (ii) the aragonitic skeleton of the interutricular space; and (iii) the equant High-Mg calcite cements of the outer rim of many of the cemented utricles (Fig. 6A). An EDX map of the segment indicates Mg is less enriched in the bladed cements as compared to the equant High-Mg calcite cements, and is comparable to the aragonite in the needle structure (Fig. 6B). This is confirmed by EDX point measurements where concentrations range between 0.4 Mol% and 1.0 Mol% for the bladed cements, whereas Mg is between 6.6 Mol% and 6.8 Mol% for the equant High-Mg calcite cements, and the aragonite needles lack detectable Mg (Fig. 6C and E, Table 1). Based on habitus and Mg content, the bladed crystals are thus interpreted as Low-Mg calcite cements.

## Mini-micritic cements

Micro-crystalline or amorphous features have been detected in specimen PPB_P3_3. Under the SEM with a maximal magnification of 30 000×, no crystal structures were identified, indicating crystal sizes smaller than 0.1 µm or an amorphous structure (Fig. 7). Accordingly, the cements here are described as 'minimicrite' following Folk (1974) and Reid & Macintyre (1998).

These cements appear darker in backscattered SEM images than the surrounding aragonitic microstructure, indicating a different mineralogy.

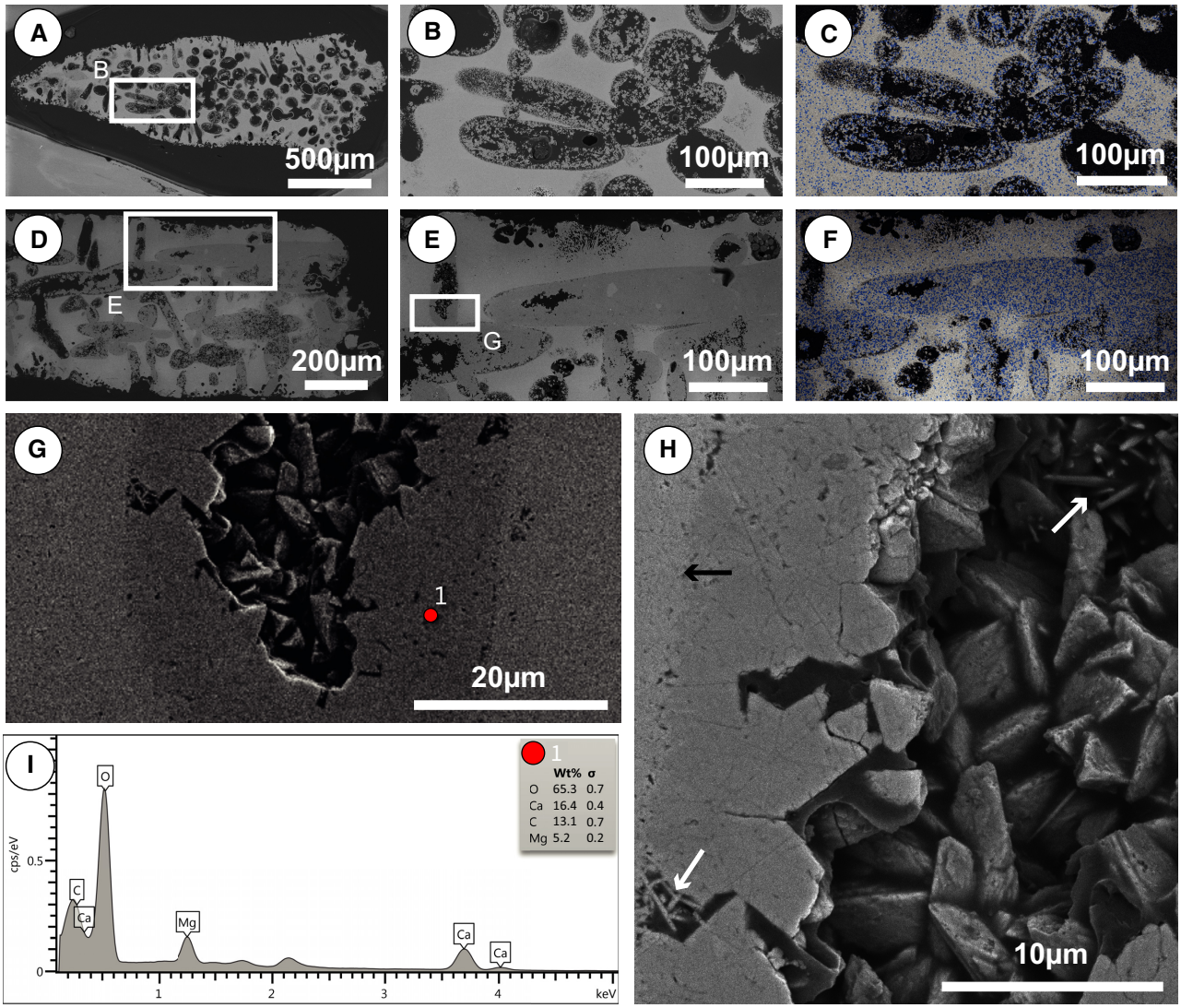


**Fig. 5.** Examples for equant High-Mg calcite cementation in utricles of *Halimeda*. (A) Overview backscattered electron image of specimen PPB17_S. (B) Close-up backscattered electron image of specimen PPB17_S showing cemented utricles. Position of the frame is indicated in (A). (C) Backscattered electron image of (B) overlain with EDX map showing the enrichment of Mg (blue pixels) in cements compared to the aragonitic interutricular space. (D) Overview backscattered electron image of specimen PPB_CP_4. (E) Close-up backscattered electron image of specimen PPB_CP_4 showing almost completely cemented utricles. Position of the frame is indicated in (D). (F) Backscattered electron image of (E) overlain with EDX map showing the enrichment of Mg (blue pixels) in cements compared to the aragonitic interutricular space. (G) Close-up backscattered electron image of a cemented utricle of specimen PPB_CP_4 showing the equant shape of cements. Position of the frame is indicated in (E). Red point indicates measurement spot of EDX spectrum shown in (I). (H) Close-up backscattered electron image of the same cemented utricle as in (G) with stronger magnification. White arrows indicate where primary aragonite needles and fibrous aragonite cements have been embedded in the equant cements. Black arrow indicates the position of the utricle rim. (I) EDX spectrum – red point in (G) – indicate that equant cements in this specimen comprise 6.2 to 6.4 Mol% Mg (see Table 1).

EDX Maps show that the concentration of Mg in the mini-micritic cements is higher than in the surrounding original aragonite skeleton (Fig. 7C), as supported by an EDX point measurement providing a Mg concentration of 3.2 to 3.3 Mol% for the minimicrite (Fig. 7G, Table 1), which points to a Low-Mg calcite mineralogy.

**Table 1.** Summary information on quantified EDX spectra. EDX provides wt% of elements that have been recalculated to Mol% by multiplying the wt% with the rounded molar mass of each element (O = 16 g/Mol, Ca = 40 g/Mol, C = 12 g/Mol, Mg = 24 g/Mol, Sr = 87.6 g/Mol), divided by the total analyzed molar mass within each measurement and multiplied by 100. Asterisks indicate those EDX spot measurements that are shown in the figures. Note that only those EDX spectra have been quantified that contain the elements O, Ca, C, Mg and Sr only, in order to determine the respective carbonate polymorph.

| Sample ID | EDX spot# | Weight% | | | | | Mol% | | | | | Morphology, mineralogy and diagenetic interpretation |
|---|---|---|---|---|---|---|---|---|---|---|---|---|
| | | O | Ca | C | Mg | Sr | O | Ca | C | Mg | Sr | |
| PPB_17S | | 53.1–54.1 | 33.7–34.5 | 6.9–7.9 | 4.8–5.0 | – | 35.2–35.5 | 56.1–56.3 | 3.5–3.8 | 4.8–4.9 | – | Equant High-Mg calcite cement |
| PPB_P1_3 | | 58.0–59.0 | 27.5–28.3 | 8.6–9.8 | 4.2–4.4 | – | 41.1–41.6 | 49.2–49.3 | 4.6–5.1 | 4.5–4.6 | – | Equant High-Mg calcite cement |
| PPB_P1_4 | | 59.0–60.2 | 23.0–23.8 | 9.7–10.9 | 6.5–6.9 | – | 43.6–44.2 | 41.2–41.4 | 5.2–5.7 | 7.0–7.2 | – | Equant High-Mg calcite cement |
| PPB_P2_7 | | 55.9–56.9 | 30.3–31.1 | 8.0–9.0 | 4.2–4.4 | – | 38.4–38.8 | 52.5–52.6 | 4.2–4.6 | 4.4–4.5 | – | Equant High-Mg calcite cement |
| PPB_P2_7 | 1 | 48.1–49.1 | 39.6–40.6 | 6.5–7.5 | 4.1–4.3 | – | 30.2–30.4 | 62.4–62.6 | 3.1–3.5 | 3.9–4.0 | – | Equant (High-) Mg calcite cement |
| PPB_P2_7 | 2 | 46.8–47.8 | 42.8–43.8 | 8.0–9.0 | – | 0.8–1.2 | 28.0–28.5 | 64.2–65.2 | 3.7–4.0 | – | 2.7–3.9 | Original aragonite skeleton |
| PPB_P2_6 | 2 | 53.9–54.9 | 38.0–39.0 | 6.6–7.6 | – | – | 34.7–35.0 | 61.7–61.7 | 3.2–3.6 | – | – | Original aragonite skeleton |
| PPB_P2_6* | 1 | 52.8–53.8 | 38.7–39.7 | 6.9–7.9 | – | – | 34.1–33.8 | 62.4–62.5 | 3.3–3.7 | – | – | Fibrous aragonite cement |
| | 2 | 54.1–55.1 | 37.4–38.4 | 6.9–7.9 | 0.0–0.2 | – | 35.0–35.4 | 61.0–61.2 | 3.4–3.8 | 0.0–0.2 | – | Fibrous aragonite cement |
| PPB_P2_4* | 3 | 47.8–48.8 | 42.7–43.7 | 6.7–7.7 | – | 1.0–1.4 | 28.5–28.9 | 63.7–64.7 | 3.0–3.4 | – | 3.3–4.5 | Original aragonite skeleton |
| PPB_P2_4 | 1 | 48.3–49.3 | 43.0–44.0 | 7.1–8.1 | 0.0–0.2 | – | 29.8–30.0 | 66.4–66.7 | 3.3–3.7 | 0.0–0.2 | – | Fibrous aragonite cement |
| | 2 | 47.6–48.6 | 42.6–43.6 | 7.8–8.8 | 0.4–0.6 | – | 29.4–29.6 | 66.0–66.3 | 3.6–4.0 | 0.4–0.6 | – | Fibrous aragonite cement |
| | 3 | 48.3–49.3 | 44.0–45.0 | 6.1–7.1 | 0–0.1 | – | 29.5–29.7 | 67.3–67.6 | 2.8–3.2 | 0–0.1 | – | Original aragonite skeleton |
| PPB_P3_3* | | 48.7–49.7 | 40.4–41.4 | 5.8–6.8 | 3.4–3.6 | – | 30.4–30.6 | 63.2–63.5 | 2.7–3.1 | 3.2–3.3 | – | Mini-micritic Low-Mg calcite cement |
| PPB_P3_1 | | 49.5–50.5 | 38.1–39.1 | 6.4–7.4 | 4.5–4.7 | – | 31.4–31.7 | 60.8–60.9 | 3.1–3.5 | 4.3–4.4 | – | Equant High-Mg calcite cement |
| PPB_CP5 | 1 | 48.0–49.2 | 28.9–29.9 | 17.3–18.7 | 3.9–4.1 | – | 34.1–34.5 | 51.9–52.0 | 9.7–9.3 | 4.2–4.3 | – | Equant High-Mg calcite cement |
| | 2 | 54.1–55.1 | 37.2–38.2 | 6.9–7.9 | 0.2–0.4 | – | 35.0–35.5 | 60.8–61.0 | 3.4–3.8 | 0.2–0.4 | – | Equant High-Mg calcite cement |
| | 3 | 53.5–54.5 | 38.9–39.9 | 6.1–7.1 | – | – | 34.2–34.4 | 62.5–62.6 | 2.9–3.3 | – | – | Original aragonite skeleton |
| PPB_CP4* | 1 | 64.6–66.0 | 16.0–16.8 | 12.4–13.8 | 5.0–5.4 | – | 52.2–53.2 | 32.9–33.2 | 7.7–8.2 | 6.2–6.4 | – | Equant High-Mg calcite cement |
| PPB_CP3* | 1 | 62.6–64.2 | 15.5–16.3 | 14.3–16.1 | 5.3–5.7 | – | 51.1–52.2 | 32.5–32.3 | 8.9–9.6 | 6.6–6.8 | – | Equant High-Mg calcite cement |
| | 2 | 64.8–67.6 | 20.5–22.3 | 10.3–13.3 | 0.3–0.9 | – | 50.2–52.2 | 41.3–41.4 | 7.4–6.2 | 0.4–1.0 | – | Bladed Low-Mg calcite cement |
| | 3 | 64.8–67.0 | 18.6–20.0 | 13.5–15.9 | – | – | 51.9–53.4 | 38.8–38.3 | 8.3–9.2 | – | – | Original aragonite skeleton |

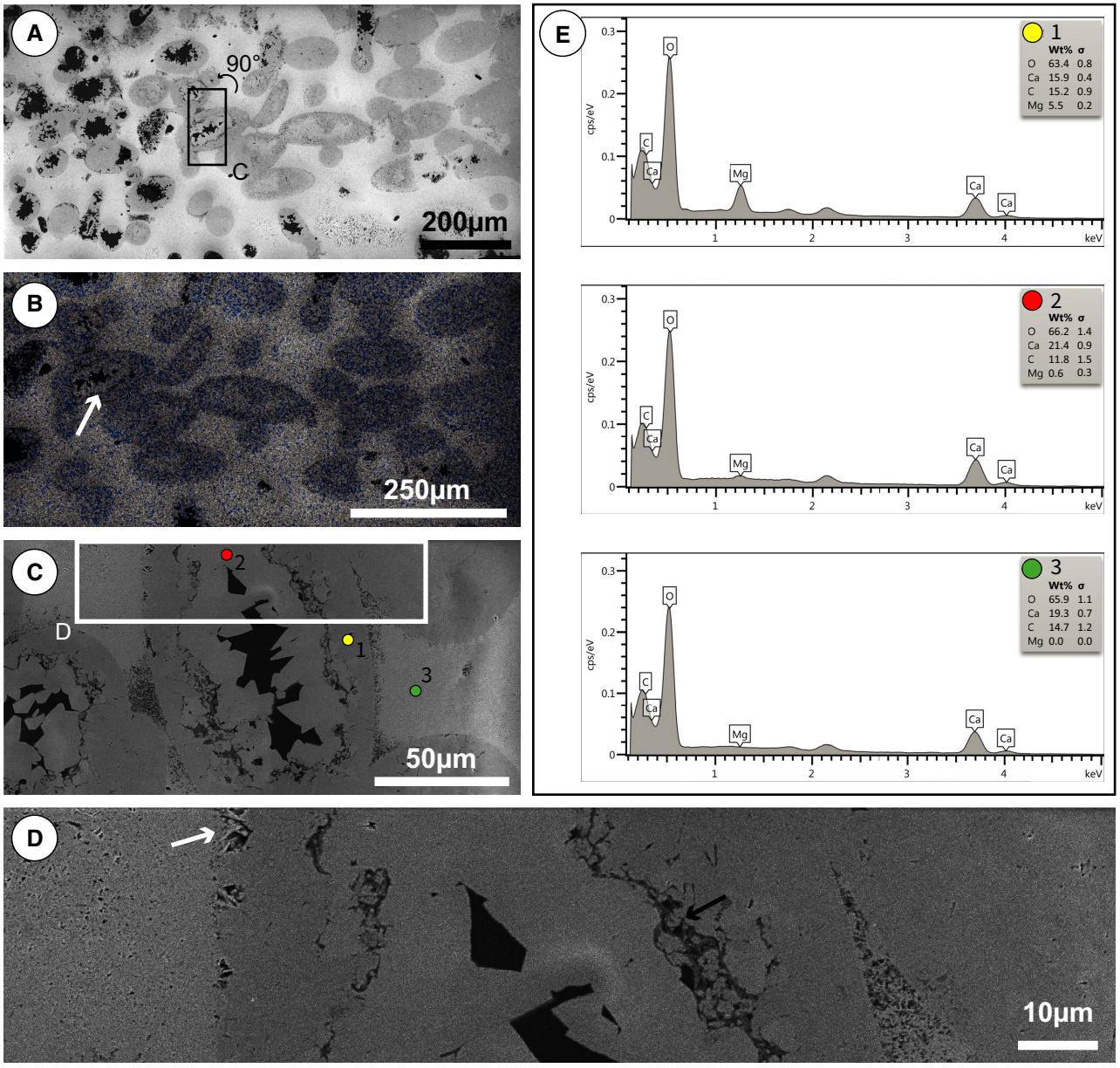


**Fig. 6.** Example of bladed Low-Mg calcite cements in utricles of *Halimeda*. (A) Overview backscattered electron image of specimen PPB_CP_3. (B) Backscattered electron image of specimen PPB_CP_3 overlain with EDX map showing the enrichment of Mg (blue pixels) in the outer rim of cemented utricles compared to the aragonitic interutricular space. White arrow indicates the boundary between two generations of cements with different concentrations of Mg. (C) Close-up backscattered electron image of one cemented utricle of specimen PPB_CP_3 where bladed cements grow on top of equant High-Mg calcite cements. Position of the frame is indicated in (A). EDX spot measurements shown in (E) are indicated by numbers '1' to '3' and the yellow, red and green spots. (D) Close-up backscattered electron image of the same cemented utricle as in (C) with higher magnification. Black arrow indicates the corroded boundary between equant High-Mg calcite cements along the outer rim of the cemented utricle and the bladed Low-Mg calcite cements. White arrow indicates that primary aragonite needles or fibrous aragonite cements have been embedded in the equant cements. (E) EDX spectra indicating the elemental composition of different generations of cements and the original skeleton: 1 = Equant High-Mg calcite; 2 = Bladed Low-Mg calcite; 3 = Aragonite.

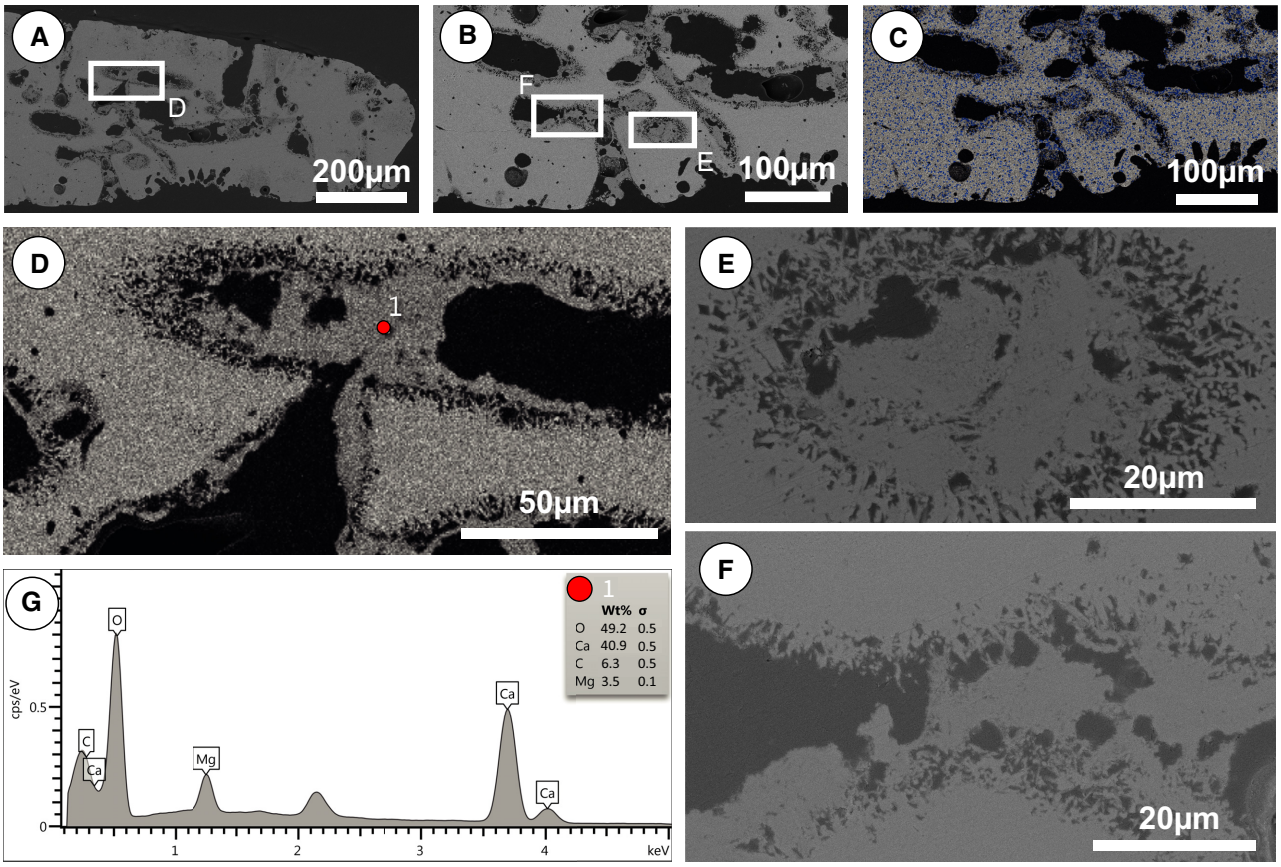


**Fig. 7.** Examples for mini-micritic Low-Mg calcite cementation in utricles of *Halimeda*. (A) Overview backscattered electron image of specimen PPB_P3_3. (B) Close-up backscattered electron image of specimen PPB_P3_3 showing cemented utricles. (C) Backscattered electron image of (B) overlain with EDX Map showing the enrichment of Mg (blue pixels) in cements compared to the aragonitic interutricular space. (D) Close-up backscattered electron image showing that mini-micritic cements are attached to fibrous aragonite cements largely without embedding them. Position of the frame is indicated in (A). Red point indicates measurement spot of EDX spectrum shown in (G). (E) and (F) Further close-up backscattered electron images showing the growth relation of mini-micritic Low-Mg calcite cements and fibrous aragonite cements. (G) EDX spectrum of the mini-micritic cements indicating a Mg concentration of 3.2 to 3.3 Mol%.

## DISCUSSION

### Early-diagenetic carbonate cementation

Segments from live *Halimeda* and those shortly after disaggregation from the alga comprise well-defined aragonitic microstructural features (Fig. 1; Wizemann *et al.*, 2014). During sediment transport across the reef flat towards the island, segments pass through a range of early-diagenetic environments (marine phreatic, marine vadose, mixing, meteoric vadose, meteoric phreatic), each of which is characterized by specific hydrological and hydrochemical conditions. In contrast to the semi-enclosed interutricular space, the micro-environmental and hydrological boundary conditions in the utricles of sedimentary *Halimeda* segments foster through flow of the ambient fluids. Accordingly, shape, mineralogy and growth relation to the substrate of diagenetic crystals within the utricles provide valuable archives of the processes that control cementation during the early stages of carbonate diagenesis in the shallow-marine, warm-water environment.

Typically, early diagenetic cementation initiates in the marine phreatic environment (Longman, 1980). The observation of fibrous aragonite cement within detrital *Halimeda* segments is in accordance to the results from earlier studies (Reid & Macintyre, 1998; Hover *et al.*, 2001). Fibrous cementation likely results from the flow of seawater that is supersaturated with respect

to carbonate (i.e. $\Omega_{Arag}$ >3; Mg : Ca ratio *ca* 5 : 1) through the utricles (Friedman *et al.*, 1974; Scoffin, 1992; Morse *et al.*, 2007), and the thermodynamically favoured aragonite nucleation and crystal growth on the aragonite substrate of the primary needles (Alexandersson, 1972; Folk, 1974). Consequently, the occurrence of fibrous aragonite cement within utricles of sedimentary *Halimeda* segments is likely the result of the interplay of inorganic parameters within the shallow-marine phreatic environment.

In contrast to the common observation of fibrous aragonite cementation in modern detrital *Halimeda* segments, occurrences of High-Mg calcite infilling utricles of *Halimeda* segments have previously merely been described from the shallow Brazilian shelf (Alexandersson & Milliman, 1981), from reef sediments of Belize (Reid & Macintyre, 1998) and from *Halimeda* bioherms in the Java Sea (Roberts *et al.*, 1988). The segments in those studies, recovered from several tens of metres to >100 m of water depth, show intragranular cements consisting of High-Mg calcite with 8 to 9 Mol% (Java Sea) and up to 13 Mol% (Brazil) $MgCO_3$, respectively. Roberts *et al.* (1988) suggested that the precipitation of High-Mg calcite cements in the Java Sea is related to the recurrent upwelling of deep-water masses undersaturated with respect to aragonite. Pulau Panambungan, located on the middle shelf, in contrast, is not reached by upwelling waters. In terms of water depth and environmental conditions, this reef flat environment is more comparable to the study site of Reid & Macintyre (1998). Furthermore, the fact that the equant High-Mg calcite cements within utricles embed fibrous aragonite cements and primary needles without dissolving them (Figs 5H and 6D) suggests that the observed High-Mg calcite cementation is not a result of dissolution of aragonite and re-precipitation of High-Mg calcite (Alexandersson & Milliman, 1981), particularly as in modern shallow-marine tropical carbonate environments under marine phreatic conditions, High-Mg calcite is rarely precipitated if the substrate is of aragonitic mineralogy (Alexandersson, 1972; Folk, 1974; Friedman *et al.*, 1974; Scoffin, 1992; Morse *et al.*, 2007).

Given & Wilkinson (1985) have suggested that High-Mg calcite precipitation in shallow-marine environments with oversaturated waters is rather controlled (besides the mineralogical template) by the rate of carbonate ion supply than by the Mg : Ca ratio of the fluid itself. Specifically, aragonite is thought to be precipitated at high carbonate supply rates, and with decreasing rates of carbonate ion supply, the mineralogy shifts to High-Mg calcite. The observation of High-Mg calcite cements in utricles embedding fibrous aragonite cements and primary needles suggests that the model proposed by Given & Wilkinson (1985) is also applicable on an intragranular scale.

Based on the observations herein and these previous studies, the authors speculate that the succession of co-occurrence of aragonite and High-Mg calcite cements in the *Halimeda* segments can be explained by the availability of $Ca^{2+}$ and $Mg^{2+}$, and the kinetics of carbonate ions that is controlled by abiotic processes. In our model, utricles in detrital *Halimeda* segments act as open pore spaces that allow for circulation of ambient seawater, for example, through tidal pumping and currents on the reef flat. Shortly after disaggregation from the alga, fluid flow rates through utricles likely are highest, resulting in the precipitation of fibrous aragonite cements. With growing crystals during ongoing aragonite cementation, the pore throat diameters and, thus, the permeability decreases. At some point, the reduced supply rate of carbonate ions will then initiate a preferential precipitation of High-Mg calcite with equant morphology (Given & Wilkinson, 1985). During this process, utricle diameters are likely to decrease irregularly, resulting in numerous 'bottle necks' with lowered permeability. Accordingly, also carbonate ion supply rates are expected to be variable within one utricle.

The formation of bladed Low-Mg calcite cements has been observed in specimen PPB_CP_3 (Fig. 6). Such cements could result from an altered pore water carbon chemistry, facilitating a shift in mineralogy through a phase segregation of the Mg : Ca ratio (Morse *et al.*, 2007). An abiotic process in the marine phreatic realm that could possibly explain such a depletion of $Mg^{2+}$-ions is the formation of a crystal druse in which remnants of pore water have been enclosed. Through ongoing equant High-Mg calcite cementation with relatively high Mg concentrations (in this study 3.9 to 7.2 Mol% Mg), the Mg : Ca ratio in the restricted environment of such a crystal druse would drop and, consequently, bladed Low-Mg calcite would form on top of the equant High-Mg calcite crystals. However, the volume of water within one restricted pore is probably not sufficient to precipitate bladed cements with dimensions such as those observed in this study (Matthews,

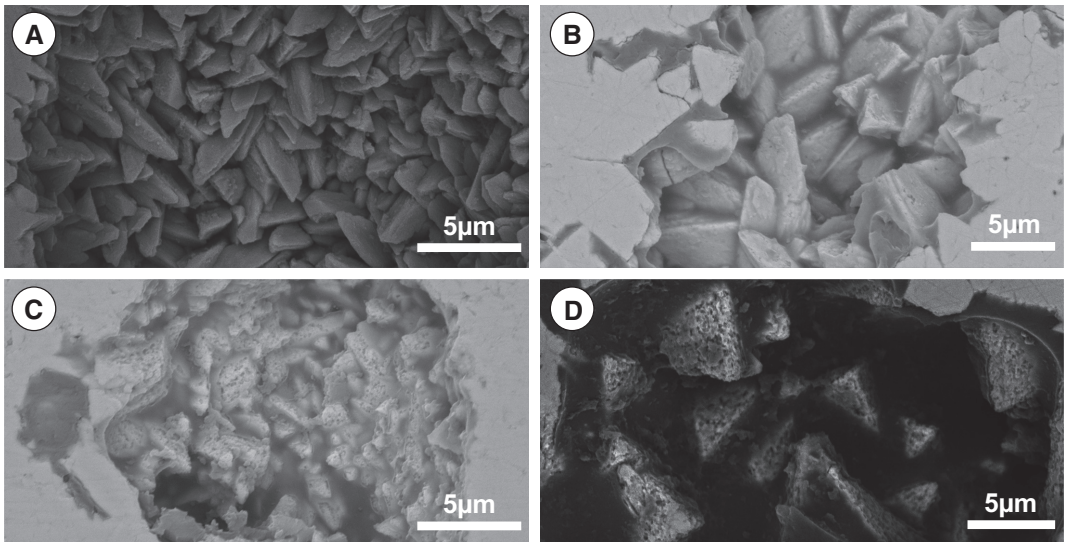


**Fig. 8.** Backscattered electron images showing different degrees of equant High-Mg calcite cement dissolution of specimens. (A) Specimen PPB_P2_7 shows no indication of equant High-Mg calcite dissolution. (B) Specimen PPB_CP_4 shows slight etching of equant High-Mg calcite dissolution. (C) and (D) Specimens PPB_P1_3 and PPB_CP_3 show obvious signs of equant High-Mg calcite etching and dissolution.

1974). Furthermore, the corrosive growth contact at the base of the bladed cements (Fig. 6D) indicates that carbonate dissolution preceded the precipitation of Low-Mg calcite cements.

It is well-known that microbial sulphate reduction related to organic matter oxidation raises pH and increases alkalinity, thus causing the precipitation of carbonate minerals (Lin *et al.*, 2018). However, during the early stages of microbial sulphate reduction, pore water becomes undersaturated with respect to carbonate due to a lowered pH (Walter & Burton, 1990; Melim *et al.*, 2002; Morse *et al.*, 2007; Gallagher *et al.*, 2012; Meister, 2013). Indeed, different degrees of equant High-Mg calcite crystal dissolution have been observed in specimens PPB_CP_3, PPB_CP_4, PPB_P2_7 and PPB_P1_3 (Fig. 8). Dissolution of biogenic carbonates often results from the interplay between carbonate mineralogy and the complexity of the respective skeletal microstructure that determines porosity and permeability (Henrich & Wefer, 1986). Etching and dissolution of equant High-Mg calcite cements containing up 7.2 Mol% Mg as a result of abiotic processes would however likely favour the re-precipitation of High-Mg calcite, not Low-Mg calcite. Accordingly, the different degrees of equant High-Mg calcite dissolution observed in several specimens in this study presumably reflect different stages of early microbial sulphate reduction, prior to the precipitation of bladed Low-Mg calcite cements.

Also the mini-micritic cements observed in this study might be a good example for microbially-triggered carbonate cementation during the early diagenesis in modern, shallow-marine, tropical reef environments. Mini-micritic cements are situated on top of fibrous aragonite cements without embedding or dissolving those (Fig. 7D, E and F). The pristine appearance of the underlying fibrous aragonite cements indicates a process other than mineral replacement for the precipitation of mini-micritic Low-Mg calcite cements.

The SEM analyses of specimen PPB_P2_4 revealed the occurrence of patchy calcite cements embedded in a non-crystalline matrix that is interpreted here to represent the remnants of extracellular polymeric substances (EPS) as produced by bacterial cells involved in biomineralization (Fig. 9A; Dupraz *et al.*, 2009; Krause *et al.*, 2018; Lin *et al.*, 2018). EDX measurements of the non-crystalline matrix detected Al, Si, K and Fe, which is untypical for shallow-marine carbonate environments in settings far from siliciclastic input. Siliciclastic minerals and crystals through dust input from the hinterland have not been detected visually in the samples studied here. It is important to note, however, that the non-crystalline matrix is

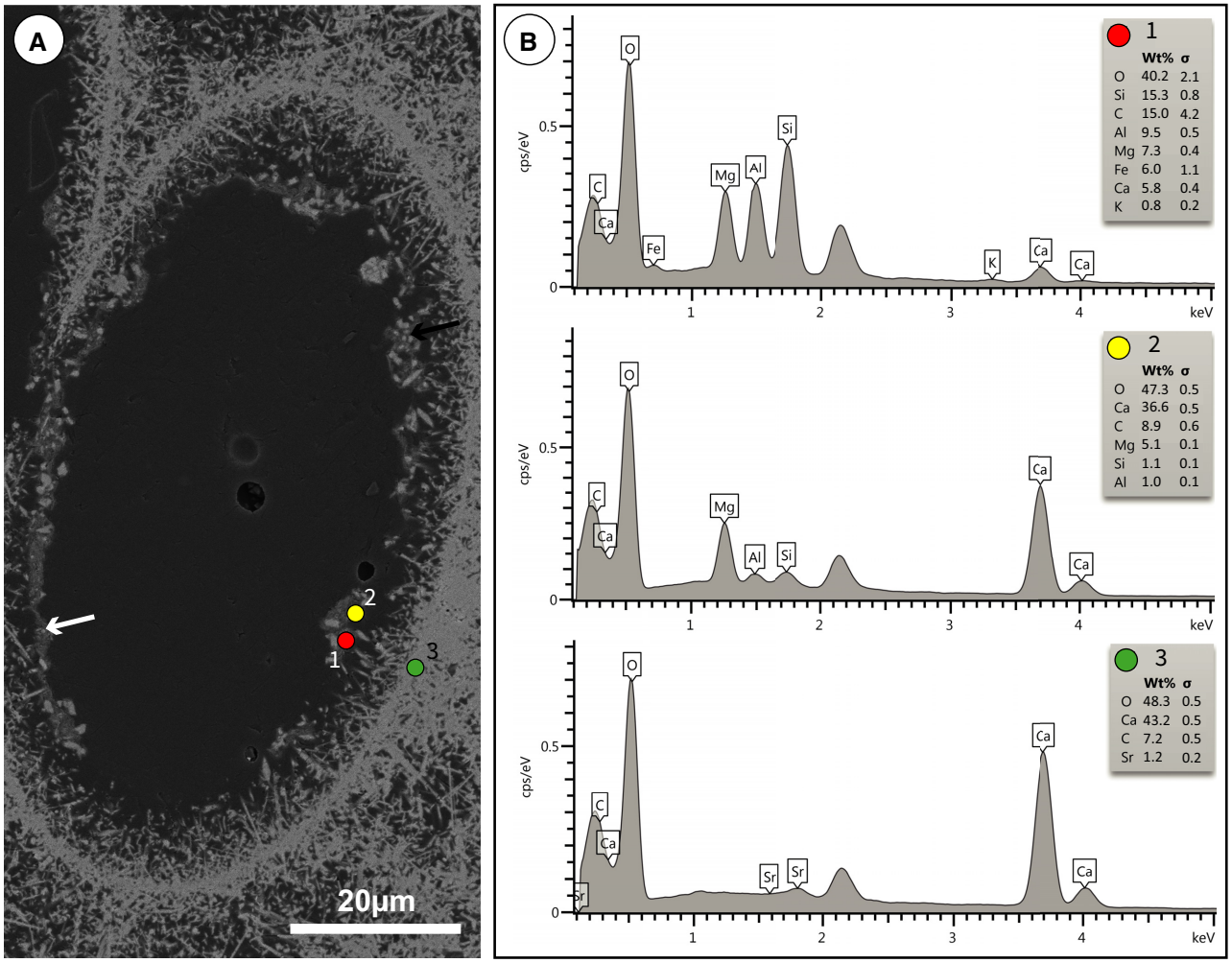


**Fig. 9.** (A) Backscattered electron image of a utricle of specimen PPB_P2_4 presumably showing how remnants of extracellular polymeric substances are attached to fibrous aragonite cements (white arrow) and embed patchy Mg calcite crystals (black arrow). EDX spot measurements shown in (B) are indicated by numbers '1' to '3' and the red, yellow and green spots. (B) EDX spot measurements: 1 = the organic matrix, presumably remnants of extracellular polymeric substances; 2 = a Mg calcite crystal within the organic matrix; 3 = the aragonitic interutricular space.

proposed to represent only remnants of the EPS, as all investigated *Halimeda* segments were collected onshore. Thus the obtained element composition would not mirror the living state of the biomineralizing organic matrix that consists of polysaccharides and amino acids (Dupraz & Visscher, 2005). The presence of elements originating from alumosilicates could accordingly be related to the persistent affinity of EPS for cation complexation onshore, as shown for subaerial environments characterized by soil formation (Curtis, 1987). The observed calcite crystals, unevenly distributed in the organic matrix, could thus be interpreted to represent the nucleation phase of Low-Mg calcite cements and the initial state of what will become the mini-micritic Low-Mg calcite precipitate, as observed in specimen PPB_P3_3 at a later stage.

Consequently, microbial activity within the utricles of *Halimeda* segments provides a possible explanation for the occurrence of both, bladed Low-Mg calcite cements that were precipitated during the later stages of microbial sulphate reduction on a corroded substrate of equant High-Mg calcite that was etched during the early stages of microbial sulphate reduction, and mini-micritic Low-Mg calcite cements. As no dissolution of aragonite needles underlying

the mini-micritic Low-Mg-calcite cements took place, cementation could therefore have been triggered either through ammonification (Krause *et al.*, 2018) or external carbonic anhydrase – or urease – activity (Seifan *et al.*, 2017; Shen *et al.*, 2017). Furthermore, the microbial decay of organic remains of the cells of *Halimeda* in the utricle walls (Böhm & Goreau, 1974; Wizemann *et al.*, 2014; Erler *et al.*, 2018) potentially influences the formation of carbonate cement.

Particularly the formation of Low-Mg calcite cements is unexpected in modern tropical shallow-water environments, however the lack of observable dissolution features of the aragonite original microstructure indicates that cementation took place in the marine phreatic environment without meteoric freshwater influence. In order to rule out any freshwater influence during the formation of the Low-Mg calcite cements, and to gain a better understanding of the specific control of certain bacterial species on the precipitated carbonate polymorph, integrated genotyping of bacteria, carbon–oxygen isotope and lipid biomarker analyses offer a potential means for detecting the underlying mechanisms for the formation of such complex successions of cements in future studies.

## Temporal assessment of cementation

Within early diagenetic environments, cementation can be a rapid process happening within a range of months to decades. Dravis (1996) showed that Holocene ooid sands on Eleuthera Island, Bahamas, have been partly cemented in less than ten years within the meteoric vadose environment. The rapidity of marine cementation has been demonstrated by Friedman (1998), who showed that ooid cementation takes place within one year in intertidal environments. A classic study on marine carbonate cementation indicated that the processes of sediment lithification are almost syndepositional, also in the shallow subtidal environment (Shinn, 1969). For the deeper marine phreatic diagenetic environment, Grammer *et al.* (1993, 1999) showed that cementation takes place within months.

Radiocarbon-dated *Halimeda* segments from this study range in age from 165 cal yr BP (PPB_CP_4) to 6164 cal yr BP (PPB_CP_3; Table 2). While a temporal assessment of cementation related to microbial activity is difficult, dating results indicate that cementation of utricles with fibrous aragonite and equant High-Mg calcite in specimen PPB_CP_4 took place since 165 cal yr BP (median age probability; Fig. 10). However, radiocarbon ages of detrital carbonate constituents indicate the timing of death of the organism. Onshore deposition, when marine cementation ultimately ceased, happened during an undefined period after 165 cal yr BP. Accordingly, the received radiocarbon dates provide maximum age constraints for the observed cement precipitation.

Conservatively assuming half of the median age probability as total transport duration would imply that ± complete cementation of utricles with either fibrous aragonite or equant High-Mg calcite takes place in less than *ca* 100 years. On the other hand, many utricles in this specimen still contain micropores between the diagenetic cements, thus indicating that complete cementation of utricles does not happen significantly faster.

If this temporal estimate is in the right order of magnitude, then intragranular carbonate cementation in the shallow-marine phreatic environment around tropical carbonate factories is more rapid than aragonite dissolution and intergranular cementation in the nearby meteoric vadose environment, as no dissolution features were observed in the investigated

**Table 2.** Radiocarbon ages and calibrated age ranges of dated *Halimeda* segments.

| Sample ID | Laboratory No. | Radiocarbon age (years BP) | Calibrated age range (2σ, calendar years BP) | Median probability (calendar years BP) |
|---|---|---|---|---|
| PPB_CP_6 | Poz-68825 | 705 ± 30 | 14–416 | 224 |
| PPB_CP_5 | Poz-68826 | 1280 ± 30 | 556–916 | 737 |
| PPB_CP_4 | Poz-68823 | 640 ± 30 | 0–338 | 165 |
| PPB_CP_3 | Poz-68822 | 5880 ± 40 | 5936–6375 | 6164 |
| PPB_CP_1 | Poz-68755 | 870 ± 60 | 144–566 | 383 |

$^{14}$C ages were calibrated to calendar years before present using the Marine20 radiocarbon age calibration curve (Heaton *et al.*, 2020) with a ΔR of −64 $^{14}$C years and an uncertainty of 70 $^{14}$C years (Southon *et al.*, 2002).

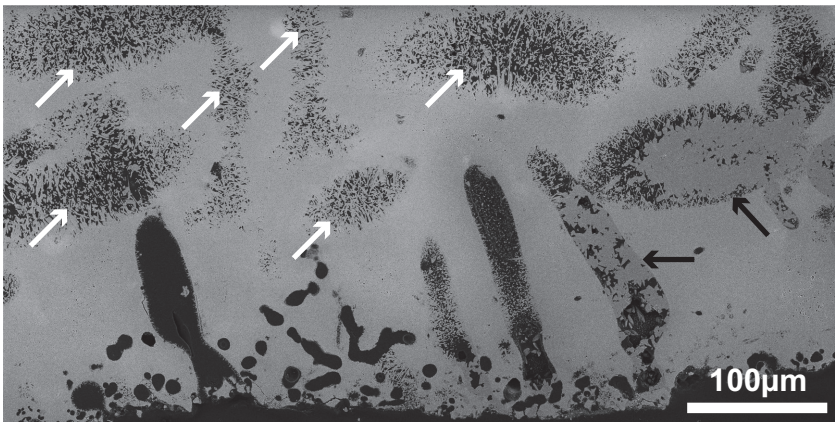


**Fig. 10.** Backscattered electron image of specimen PPB_CP_4 showing the co-occurrence of utricles cemented with either fibrous aragonite (white arrows) or equant High-Mg calcite (black arrows).

*Halimeda* specimens, and all analyzed sediment samples were unlithified. This assessment of temporal dimensions of processes (cementation versus dissolution and re-precipitation) dominating within different diagenetic zones needs, however, to be tested with further radiometric data from different carbonate constituents. Particularly in comparison to the marine vadose/mixing zone environment, which is characterized by rapid lithification resulting from dissolution related to the degradation of organic matter and high rates of evaporation, and which corresponds to the zone of beachrock formation along the south-eastern island margin (Figs 2 and 3; Melim *et al.*, 2004).

The radiocarbon ages of dated *Halimeda* segments are in a comparable range as the results presented by Shinn (1969) for submarine lithification in the Persian Gulf. The longer time spans for cementation presented in this study and by Shinn (1969) compared to previous results (Grammer *et al.*, 1993; Dravis, 1996; Friedman, 1998; Grammer *et al.*, 1999) could be related to a particularly high saturation state ($\Omega_{Arag} > 4$) around the Bahamas archipelago and strong currents at the slope that pump much larger quantities of supersaturated water through the pores and consequently fosters rapid cementation. Furthermore, works from the Bahamas have typically used ooids as study material, which are carbonate constituents with particularly smooth surfaces and an accordingly high intergranular permeability, thus additionally triggering cementation. Results from this study indicate that early diagenetic cementation in a tropical shallow-marine phreatic environment with $\Omega_{Arag} \leq 4$ proceeds somewhat slower for the majority of biogenic carbonate constituents.

## CONCLUSIONS

This study presents the results from a petrographic analysis of detrital *Halimeda* segments collected on a mid-shelf reef island in the Spermonde Archipelago, Indonesia. From 27 analyzed segments, 17 have utricles infilled with carbonate cements. On the basis of crystal shapes and quantitative EDX element measurements, the cements were classified into fibrous aragonite, equant High-Mg calcite (3.9 to 7.2 Mol% Mg), bladed Low-Mg calcite (0.4 to 1.0 Mol% Mg) and minimicritic Low-Mg calcite (crystal size <0.1 µm; 3.2 to 3.3 Mol% Mg). On the basis of crystal appearance and growth relations to the substrate, it is inferred that fibrous aragonite and equant High-Mg calcite cement precipitation results from largely abiotic processes related to pore water chemistry, kinetics and carbonate ion supply rates. Conversely, the precipitation of bladed and minimicritic Low-Mg calcite cements is thought to result from degradation of organic matter and microbial sulphate reduction. The precipitation of marine Low-Mg calcite cements must involve a fractionating component that would be difficult to explain by purely abiotic processes. Accordingly, this study provides a good example of the overlying effects of physico-chemical and biological processes on early-diagenetic carbonate cementation and provides indications for early-diagenetic Low-Mg calcite cementation in the absence of meteoric freshwater influence. Consequently, results of this study suggest that internal cementation of microstructurally complex carbonate constituents comprise highly diverse precipitates that form early during the sedimentary cycle. While aragonite and High-Mg calcite cements likely convert to Low-Mg calcite during

later stages of meteoric and burial diagenesis, the recognition of potentially early-diagenetic, marine Low-Mg calcite cements could be helpful when the diagenetic history of fossil carbonate platforms is interpreted.

## ACKNOWLEDGEMENTS

TM and YK acknowledge financial support through a grant from the Deutsche Forschungsgemeinschaft (MA 6967/2-1). The Leibniz-Centre for Tropical Marine Research (ZMT) has provided lab support. Fieldwork has been conducted with permission from the Indonesian Ministry for Research and Technology (Research Permit No. 399/SIP/ FRP/SM/X/2012 and Working Permit No. 2C11JD5741-L). We thank Gene Rankey and two additional reviewers for their suggestions that helped to improve this paper. Open Access funding enabled and organized by Projekt DEAL.
[Correction added on 8 October 2021 after first publication: Projekt Deal funding statement has been added in acknowledgements section.]

## DATA AVAILABILITY STATEMENT

Raw SEM images analyzed for this study have been uploaded to the data repository PANGAEA and can be accessed at https://doi.pangaea.de/10.1594/PANGAEA.923980

## REFERENCES

**Alexandersson, E.** and **Milliman, J.** (1981) Intragranular Mg-calcite cement in Halimeda plates from the Brazilian continental shelf. *J. Sediment. Res.*, **51**, 1309–1314.

**Alexandersson, T.** (1972) Intragranular growth of marine aragonite and Mg-calcite; evidence of precipitation from supersaturated seawater. *J. Sediment. Res.*, **42**, 441–460.

**Bathurst, R.G.** (1966) Boring algae, micrite envelopes and lithification of molluscan biosparites. *Geol. J.*, **5**, 15–32.

**Bathurst, R.G.** (1971) *Carbonate Sediments and their Diagenesis. Developments in Sedimentology 12* 1st Edition, pp.1–658. Elsevier, Amsterdam.

**Bender, M.**, **Mann, T.**, **Stocchi, P.**, **Kneer, D.**, **Schöne, T.**, **Illigner, J.**, **Jompa, J.** and **Rovere, A.** (2020) Late Holocene (0–6 ka) sea-level changes in the Makassar Strait, Indonesia. *Clim. Past.*, **16**, 1187–1205.

**Böhm, E.L.** and **Goreau, T.F.** (1974) The determination of calcium-45 in sea water, corals and calcareous algae by liquid scintillation counting. *Trans. R. Soc. S. Afr.*, **41**, 25–32. https://doi.org/10.1080/00359197409519436

**Burton, E.A.** (1993) Controls on marine carbonate cement mineralogy: review and reassessment. *Chem. Geol.*, **105**, 163–179.

**Curtis, C.** (1987) Mineralogical consequences of organic matter degradation in sediments: inorganic/organic diagenesis. In: *Marine Clastic Sedimentology* (Eds. Legget, J.K. and Zuffa, G.G.), pp. 108–123. Springer, Dordrecht. https://doi.org/10.1007/978-94-009-3241-8_6

**Dravis, J.J.** (1996) Rapidity of freshwater calcite cementation—implications for carbonate diagenesis and sequence stratigraphy. *Sed. Geol.*, **107**, 1–10.

**Dupraz, C.** and **Visscher, P.T.** (2005) Microbial lithification in marine stromatolites and hypersaline mats. *Trends Microbiol.*, **13**, 429–438.

**Dupraz, S.**, **Parmentier, M.**, **Ménez, B.** and **Guyot, F.** (2009) Experimental and numerical modeling of bacterially induced pH increase and calcite precipitation in saline aquifers. *Chem. Geol.*, **265**, 44–53.

**Erler, D.V.**, **Nothdurft, L.**, **McNeil, M.** and **Moras, C.A.** (2018) Tracing nitrate sources using the isotopic composition of skeletal-bound organic matter from the calcareous green algae Halimeda. *Coral Reefs*, **37**, 1003–1011. https://doi.org/10.1007/s00338-018-01742-z

**Flügel, E.** (2004) *Microfacies of Carbonate Rocks: Analysis, Interpretation and Application*. Springer Science & Business Media, Berlin Heidelberg New York.

**Folk, R.L.** (1965) Some aspects of recrystallization in ancient limestones. In: *Dolomitization and Limestone Diagenesis, Vol. 13, Society for Sedimentary Geology* (Eds. Pray, L.C. and Murray, R.C.), Special Publications, pp. 14–48. http://dx.doi.org/10.2110/pec.65.07.0014

**Folk, R.L.** (1974) The natural history of crystalline calcium carbonate; effect of magnesium content and salinity. *J. Sediment. Res.*, **44**, 40–53.

**Friedman, G.M.** (1998) Rapidity of marine carbonate cementation—implications for carbonate diagenesis and sequence stratigraphy: perspective. *Sed. Geol.*, **119**, 1–4.

**Friedman, G.M.**, **Amiel, A.J.** and **Schneidermann, N.** (1974) Submarine cementation in reefs; example from the Red Sea. *J. Sediment. Res.*, **44**, 816–825.

**Gacutan, J.**, **Vila-Concejo, A.**, **Nothdurft, L.D.**, **Fellowes, T.E.**, **Cathey, H.E.**, **Opdyke, B.N.**, **Harris, D.l.**, **Hamylton, S.**, **Carvalho, R.C.**, **Byrne, M.** and **Webster, J.M.** (2017) Mg/Ca and Sr/Ca as novel geochemical proxies for understanding sediment transport processes within coral reefs. *Estuar. Coast. Shelf Sci.*, **197**, 54–68. https://doi.org/10.1016/j.ecss.2017.08.010

**Gallagher, K.L.**, **Kading, T.J.**, **Braissant, O.**, **Dupraz, C.** and **Visscher, P.T.** (2012) Inside the alkalinity engine: the role of electron donors in the organomineralization potential of sulfate-reducing bacteria. *Geobiology*, **10**, 518–530.

**Given, R.K.** and **Wilkinson, B.H.** (1985) Kinetic control of morphology, composition, and mineralogy of abiotic sedimentary carbonates. *J. Sediment. Res.*, **55**, 109–119.

**Grammer, G.M.**, **Crescini, C.M.**, **McNeill, D.F.** and **Taylor, L.H.** (1999) Quantifying rates of syndepositional marine cementation in deeper platform environments-new insight into a fundamental process. *J. Sediment. Res.*, **69**, 202–207.

**Grammer, G.M.**, **Ginsburg, R.N.**, **Swart, P.K.**, **McNeill, D.F.**, **Jull, A.T.** and **Prezbindowski, D.R.** (1993) Rapid growth rates of syndepositional marine aragonite cements in steep marginal slope deposits, Bahamas and Belize. *J. Sediment. Res.*, **63**, 983–989.

**Heaton, T.J.**, **Köhler, P.**, **Butzin, M.**, **Bard, E.**, **Reimer, R.W.**, **Austin, W.E.N.**, **Bronk Ramsey, C.**, **Grootes, P.M.**, **Hughen, K.A.**, **Kromer, B.**, **Reimer, P.J.**, **Adkins, J.**, **Burke, A.**, **Cook, M.S.**, **Olsen, J.** and **Skinner, L.C.** (2020) Marine20—The marine radiocarbon age calibration curve

(0–55,000 cal BP). *Radiocarbon*, **62**(4), 779–820. http://dx.doi.org/10.1017/rdc.2020.68

**Henrich, R.** and **Wefer, G.** (1986) Dissolution of biogenic carbonates: effects of skeletal structure. *Mar. Geol.*, **71**, 341–362.

**Hillis-Colinvaux, L.** (1980) Ecology and taxonomy of Halimeda: primary producer of coral reefs. In *Advances In Marine Biology*, Vol. **17**, pp. 1–327. Elsevier, London.

**Hover, V.C.**, **Walter, L.M.** and **Peacor, D.R.** (2001) Early marine diagenesis of biogenic aragonite and Mg-calcite: new constraints from high-resolution STEM and AEM analyses of modern platform carbonates. *Chem. Geol.*, **175**, 221–248.

**Janßen, A.**, **Wizemann, A.**, **Klicpera, A.**, **Satari, D.Y.**, **Westphal, H.** and **Mann, T.** (2017) Sediment composition and facies of Coral Reef Islands in the spermonde archipelago, Indonesia. *Front. Mar. Sci.*, **4**. https://doi.org/10.3389/fmars.2017.00144

**Johns, H.D.** and **Moore, C.H.** (1988) Reef to basin sediment transport using Halimeda as a sediment tracer, Grand Cayman Island, West Indies. *Coral Reefs*, **6**, 187–193.

**Kench, P.S.**, **Chan, J.**, **Owen, S.** and **McLean, R.** (2014) The geomorphology, development and temporal dynamics of Tepuka Island, Funafuti atoll, Tuvalu. *Geomorphology*, **222**, 46–58.

**Kench, P.S.** and **Thomas, M.** (2017) Reef Island evolution and dynamics: insights from the Indian and Pacific Oceans and perspectives for the spermonde archipelago. *Front. Mar. Sci.*, **4**. https://doi.org/10.3389/fmars.2017.00145

**Kench, P.S.**, **McLean, R.F.** and **Nichol, S.L.** (2005) New model of reef-island evolution: Maldives, Indian Ocean. *Geology*, **33**, 145.

**Kendall, C.G.S.C.** and **Skipwith, P.A.E.** (1969) Holocene shallow-water carbonate and evaporite sediments of Khor al Bazam, Abu Dhabi, southwest Persian Gulf. *AAPG Bull.*, **53**, 841–869.

**Krause, S.**, **Liebetrau, V.**, **Löscher, C.**, **Böhm, F.**, **Gorb, S.**, **Eisenhauer, A.** and **Treude, T.** (2018) Marine ammonification and carbonic anhydrase activity induce rapid calcium carbonate precipitation. *Geochim. Cosmochim. Acta*, **243**, 116–132.

**Lin, C.Y.**, **Turchyn, A.V.**, **Steiner, Z.**, **Bots, P.**, **Lampronti, G.I.** and **Tosca, N.J.** (2018) The role of microbial sulfate reduction in calcium carbonate polymorph selection. *Geochim. Cosmochim. Acta*, **237**, 184–204.

**Longman, M.W.** (1980) Carbonate diagenetic textures from nearsurface diagenetic environments. *AAPG Bull.*, **64**, 461–487.

**Mann, T.**, **Bender, M.**, **Lorscheid, T.**, **Stocchi, P.**, **Vacchi, M.**, **Switzer, A.D.** and **Rovere, A.** (2019) Holocene sea levels in southeast Asia, Maldives, India and Sri Lanka: the SEAMIS database. *Quatern. Sci. Rev.*, **219**, 112–125.

**Mann, T.**, **Rovere, A.**, **Schöne, T.**, **Klicpera, A.**, **Stocchi, P.**, **Lukman, M.** and **Westphal, H.** (2016) The magnitude of a mid-Holocene sea-level highstand in the Strait of Makassar. *Geomorphology*, **257**, 155–163.

**Matthews, R.** (1974) A process approach to diagenesis of reefs and reef associated limestones. In: *Reefs in time and space: Society of Economic Paleontologists and Mineralogists Special Publication* (Ed. Laporte, L.F.), Vol.**18**, pp. 234–256. Society of Economic Paleontologists and Mineralogists, Tulsa, OK. https://doi.org/10.2110/pec.74.18.0234

**Meister, P.** (2013) Two opposing effects of sulfate reduction on carbonate precipitation in normal marine, hypersaline, and alkaline environments. *Geology*, **41**, 499–502.

**Melim, L.A.**, **Swart, P.K.** and **Eberli, G.P.** (2004) Mixing-zone diagenesis in the subsurface of Florida and the Bahamas. *J. Sediment. Res.*, **74**, 904–913.

**Melim, L.**, **Westphal, H.**, **Swart, P.**, **Eberli, G.** and **Munnecke, A.** (2002) Questioning carbonate diagenetic paradigms: evidence from the Neogene of the Bahamas. *Mar. Geol.*, **185**, 27–53.

**Morse, J.W.**, **Arvidson, R.S.** and **Lüttge, A.** (2007) Calcium carbonate formation and dissolution. *Chem. Rev.*, **107**, 342–381.

**Multer, H.G.** (1988) Growth rate, ultrastructure and sediment contribution of Halimeda incrassata and Halimeda monile, Nonsuch and Falmouth Bays, Antigua, WI. *Coral Reefs*, **6**, 179–186.

**Pomar, L.** (2001) Types of carbonate platforms: a genetic approach. *Basin Res.*, **13**, 313–334.

**Pomar, L.**, **Baceta, J.I.**, **Hallock, P.**, **Mateu-Vicens, G.** and **Basso, D.** (2017) Reef building and carbonate production modes in the west-central Tethys during the Cenozoic. *Mar. Pet. Geol.*, **83**, 261–304.

**Pomar, L.**, **Bassant, P.**, **Brandano, M.**, **Ruchonnet, C.** and **Janson, X.** (2012a) Impact of carbonate producing biota on platform architecture: insights from Miocene examples of the Mediterranean region. *Earth Sci. Rev.*, **113**, 186–211.

**Pomar, L.**, **Brandano, M.** and **Westphal, H.** (2004) Environmental factors influencing skeletal grain sediment associations: a critical review of Miocene examples from the western Mediterranean. *Sedimentology*, **51**, 627–651.

**Pomar, L.** and **Hallock, P.** (2008) Carbonate factories: a conundrum in sedimentary geology. *Earth Sci. Rev.*, **87**, 134–169.

**Pomar, L.** and **Haq, B.U.** (2016) Decoding depositional sequences in carbonate systems: Concepts vs experience. *Global Planet. Change*, **146**, 190–225.

**Pomar, L.** and **Kendall, C.** (2008) Architecture of carbonate platforms: a response to hydrodynamics and evolving ecology. In: *Controls on Carbonate Platform and Reef Development* (Eds. Lukasik, J. and Simo, J.A.), **89**, 187–216. SEPM Special Publication.

**Pomar, L.**, **Morsilli, M.**, **Hallock, P.** and **Bádenas, B.** (2012b) Internal waves, an under-explored source of turbulence events in the sedimentary record. *Earth Sci. Rev.*, **111**, 56–81.

**Rees, S.**, **Opdyke, B.**, **Wilson, P.** and **Henstock, T.** (2007) Significance of Halimeda bioherms to the global carbonate budget based on a geological sediment budget for the Northern Great Barrier Reef, Australia. *Coral Reefs*, **26**, 177–188.

**Reid, R.P.** and **Macintyre, I.G.** (1998) Carbonate recrystallization in shallow marine environments: a widespread diagenetic process forming micritized grains. *J. Sediment. Res.*, **68**, 928–946.

**Reid, R.P.** and **Macintyre, I.G.** (2000) Microboring versus recrystallization: further insight into the micritization process. *J. Sediment. Res.*, **70**, 24–28.

**Renema, W.** and **Troelstra, S.R.** (2001) Larger foraminifera distribution on a mesotrophic carbonate shelf in SW Sulawesi (Indonesia). *Palaeogeogr. Palaeoclimatol. Palaeoecol.*, **175**, 125–146.

**Roberts, H.**, **Aharon, P.** and **Phipps, C.** (1988) Morphology and sedimentology of Halimeda bioherms from the eastern Java Sea (Indonesia). *Coral Reefs*, **6**, 161–172.

**Scholle, P.A.** and **Ulmer-Scholle, D.S.** (2003) *A Color Guide to the Petrography of Carbonate Rocks: Grains, Textures, Porosity, Diagenesis, AAPG Memoir 77*. AAPG, Tulsa, OK.

**Scoffin, T.** (1992) Taphonomy of coral reefs: a review. *Coral Reefs*, **11**, 57–77.

**Seifan, M.**, **Samani, A.K.** and **Berenjian, A.** (2017) New insights into the role of pH and aeration in the bacterial production of calcium carbonate (CaCO 3). *Appl. Microbiol. Biotechnol.*, **101**, 3131–3142.

**Shen, T.**, **Li, W.**, **Pan, W.**, **Lin, S.**, **Zhu, M.** and **Yu, L.** (2017) Role of bacterial carbonic anhydrase during CO2 capture in the CO2-H2O-carbonate system. *Biochem. Eng. J.*, **123**, 66–74.

**Shinn, E.A.** (1969) Submarine lithification of Holocene carbonate sediments in the Persian Gulf. *Sedimentology*, **12**, 109–144. https://doi.org/10.1111/j.1365-3091.1969.tb00166.x

**Southon, J.**, **Kashgarian, M.**, **Fontugne, M.**, **Metivier, B.** and **Yim, W.W.** (2002) Marine reservoir corrections for the Indian Ocean and Southeast Asia. *Radiocarbon*, **44**, 167–180.

**Summons, R.**, **Bird, L.**, **Gillespie, A.**, **Pruss, S.**, **Roberts, M.** and **Sessions, A.** (2013) Lipid biomarkers in ooids from different locations and ages: evidence for a common bacterial flora. *Geobiology*, **11**, 420–436.

**Tucker, M.** and **Bathurst, R.** (1990) Marine diagenesis: modern and ancient. In: *Carbonate Diagenesis* (Eds. Tucker, M. and Bathurst, R.), **1**, pp. 1–9. Blackwell Scientific Publications, Oxford. https://onlinelibrary.wiley.com/doi/book/10.1002/9781444304510

**Umbgrove, J.** (1928) De koraalriffen van den Spermonde-Archipel (Zuid-Celebes). *Leidse. Geol. Meded.*, **3**, 228–247.

**Walter, L.M.** and **Burton, E.A.** (1990) Dissolution of recent platform carbonate sediments in marine pore fluids. *Am. J. Sci.*, **290**, 601–643.

**Wentworth, C.K.** (1922) A scale of grade and class terms for clastic sediments. *J. Geol.*, **30**, 377–392.

**Wizemann, A.**, **Mann, T.**, **Klicpera, A.** and **Westphal, H.** (2015) Microstructural analyses of sedimentary Halimeda segments from the Spermonde Archipelago (SW Sulawesi, Indonesia): a new indicator for sediment transport in tropical reef islands? *Facies*, **61**, 4.

**Wizemann, A.**, **Meyer, F.W.** and **Westphal, H.** (2014) A new model for the calcification of the green macro-alga Halimeda opuntia (Lamouroux). *Coral Reefs*, **33**, 951–964.

**Wizemann, A.**, **Nandini, S.D.**, **Stuhldreier, I.**, **Sánchez-Noguera, C.**, **Wisshak, M.**, **Westphal, H.**, **Rixen, T.**, **Wild, C.** and **Reymond, C.E.** (2018) Rapid bioerosion in a tropical upwelling coral reef. *PLoS One*, **13**, e0202887.

**Woodroffe, C.**, **McLean, R.**, **Smithers, S.** and **Lawson, E.** (1999) Atoll reef-island formation and response to sea-level change: West Island, Cocos (Keeling) Islands. *Mar. Geol.*, **160**, 85–104.

*Manuscript received 26 August 2020; revision accepted 28 July 2021*